Photothermal synergistic catalytic oxidation of ethyl acetate over MOFs-derived mesoporous N-TiO$_2$ supported Pd catalysts

Xun Wang [a], Linke Wu [a], Zhiwei Wang [a], Ying Feng [a], Yuxi Liu [a], Hongxing Dai [a], Zhihua Wang [b,*], Jiguang Deng [a,*]

[a] *Beijing Key Laboratory for Green Catalysis and Separation, Key Laboratory of Beijing on Regional Air Pollution Control, Key Laboratory of Advanced Functional Materials, Education Ministry of China, Department of Environmental Chemical Engineering, School of Environmental and Chemical Engineering, Faculty of Environment and Life, Beijing University of Technology, Beijing 100124, China*
[b] *State Key Laboratory of Chemical Resource Engineering, Beijing University of Chemical Technology, Beijing 100029, China*

ARTICLE INFO

ABSTRACT

To overcome the main challenge of low photocatalytic efficiency and high energy consumption of thermocatalysis in the oxidation of volatile organic compounds (VOCs), MOF-derived mesoporous disk-like yPd/xN-TiO$_2$ (x = 3.2, 5.5, 7.7 wt%, and y = 0.26 wt%) were prepared by ball milling-calcination method for photothermal catalytic oxidation of ethyl acetate. Morphological and pore structure characterization indicated that Pd/N-TiO$_2$ had abundant pore structure and large specific surface area, which facilitated the adsorption of pollutants on the active sites. Among the catalysts, 0.26 Pd/3.2 N-TiO$_2$ exhibited optimal photothermal catalytic performance. The corresponding temperature required for 50% and 90% conversion of ethyl acetate was 192 and 212 °C, with the specific reaction rate of 0.95 μmol/(g$_{Pd}$ s) at 150 °C. Doping of N and loading of Pd nanoparticles enhanced the light absorption capacity, promoted the charge separation, and the adsorption capacity of ethyl acetate, resulting in a high photothermal catalytic oxidation activity. The detection of free radicals indicated that the photothermal synergy was associated with the generation of reactive oxygen species over 0.26 Pd/3.2 N-TiO$_2$ under light irradiation condition, which directly participated in the catalytic removal of ethyl acetate. A proper increase in temperature could also promote the migration of carriers. The photothermal catalytic oxidation of VOCs over MOF-derivatives had great potential application for environmental protection.

1. Introduction

Volatile organic compounds (VOCs) are closely associated with the formation of photochemical smog, ozone and so on, threatening the ecological environment and human health [1–3]. Ethyl acetate (EA) is a common VOCs and used in the coating, ink, pharmaceutical and automobile manufacturing industry [4]. Among the treatment technologies, catalytic oxidation, which has advantages such as high activity and low secondary pollution, is widely used in the removal of low concentration VOCs or selective oxidation of VOCs [5]. However, high energy consumption is a serious problem in terms of catalytic oxidation [6]. Although photocatalysis also has certain potential on VOCs removal, it suffers from problems such as low quantum yield [7]. To overcome the above shortcomings and maximize the synergy, the combination of thermocatalysis and photocatalysis has become a new research point [8,9]. For instance, Pt/TiO$_2$-WO$_3$ had high photothermal catalytic activity

for the oxidation of propane, due to the generation of oxygen intermediate (O$_2^-$) on the catalyst [10]. Because of the synergistic effect of photocatalysis and thermocatalysis, n-pentane could be fully mineralized over PtCu/CeO$_2$ under irradiation at 400 °C, which was 200 °C lower than the thermocatalytic oxidation alone. Thermal catalysis was beneficial to alleviate the influence of carbon deposition. PtCu/CeO$_2$ had strong light absorption ability and electron-hole separation ability. The photothermal synergy made it have high catalytic performance and stability [11].

Metal-organic frameworks (MOFs) are porous materials with periodic network frameworks, and widely used in adsorption [12], sensing [13], catalysis [14]. Due to the abundant and ordered channels of MOFs, which are favorable for the transport of target pollutants and the release of intermediates, they are considered as ideal precursors for the preparation of porous metal oxides (PMOs)[15]. The metal nodes and organic ligands of MOFs can be in situ converted into metal oxides, thus

maintaining the porosity of MOFs after derivatization treatment [16]. For example, rod-like porous Co_3O_4 derived from Co-MOFs possessed excellent performance for o-xylene removal [17]. The crossed channel structure of MnO_x-CeO_2 derived from Ce-BTC made its large specific surface area and Frankel oxygen vacancy (F-OVs) recovery potential, which ensured MnO_x-CeO_2 had high performance for ethyl acetate removal at high space velocity [18]. MIL-125 as a typical Ti-based MOFs exhibited good thermal stability and large specific surface area [19]. The three-dimensional arrangement of octanuclear Ti-clusters could form octahedral vacancies, which allowed easy access for guest molecules. Porous TiO_2 or TiO_2/C composites derived from MIL-125(Ti) were widely used in electrodes [20], lithium-ion batteries [21], photocatalytic degradation of Rhodamine B [22] and oxidation of dibenzothiophene [23].

In view of the advantages of photothermal catalysis and MOFs in the preparation of porous metal oxides, we herein used MIL-125(Ti) to prepare the yPd/xN-TiO_2 (y = 0.26 wt%, x = 3.2, 5.5 and 7.7 wt%) catalysts for the photothermal catalytic oxidation of ethyl acetate. The 0.26 Pd/3.2 N-TiO_2 catalyst exhibited excellent photothermal catalytic oxidation activity and stability. In addition, possible reaction mechanism of photothermal catalytic oxidation of ethyl acetate was also proposed.

2. Experimental

2.1. Chemicals

Methanol (MeOH), dimethylformamide (DMF) and melamine were obtained from the J&K Scientific Co., Ltd. Tetrabutyl titanate and 1,4-benzenedicarboxylic acid (H_2BDC) were received from Alfa Aesar Co., Ltd. Palladium nitrate was obtained from the Innochem Company. P25 was purchased from the Evonik Industries. All of the chemicals were used without further purification.

2.2. Catalyst Preparation

Synthesis of MIL-125(Ti) 2.2 g H_2BDC was introduced in a solution containing 36 mL DMF and 4 mL MeOH, and stirred for 10 min at room temperature. Then, 2.4 mL tetrabutyl titanate was added into the suspension and stirred for 15 min. The suspension was sealed in the 100 mL Teflon-lined autoclave for solvothermal treatment at 150 °C for 48 h. Finally, MIL-125(Ti) was obtained after filtration, washing twice with MeOH and drying at 120 °C for 12 h.

2.3. Preparation of Pd/N-TiO₂

First, a certain amount of palladium nitrate solution was dropped to 0.3 g of MIL-125 powder. After drying, mixed powders of MIL-125(Ti) and different qualities of melamine were ground in a Nanjing Nanda planet-type grinding mill system at 30 Hz for 15 min. The as-obtained powders were calcined in air from room temperature to 500, 600 and 700 °C (10 °C/min) and hold for 300 min. The samples were named as TiO_2-T, xN-TiO_2-T or yPd/xN-TiO_2-T (x = 3.2, 5.5 and 7.7 wt%, the actual percentage of N measured by the elemental analyzer. y = 0.05, 0.10 and 0.26 wt%, the actual loading of Pd. T indicated different calcination temperatures). The 0.24 Pd/TiO_2-500 and 0.26 Pd/3.2 N-P25–500 samples were prepared via the same method, except that melamine was not added for 0.24 Pd/TiO_2-500, and MIL-125(Ti) was replaced with commercial P25 for 0.26 Pd/3.2 N-P25–500.

2.4. Catalyst characterization

The inductively coupled plasma-atomic emission spectroscopic (ICP-AES) technique was used to determine the actual Pd contents in each samples. X-ray diffraction (XRD) patterns were measured on a Bruker D8 Advance diffractometer with Cu Kα radiation and nickel filter.

Transmission electron microscopic (TEM) and high resolution transmission electron microscopic (HRTEM) images as well as element mappings of the samples were obtained on the equipment FEI G2 80–200/Chemi-STEM. Surface area measurements were carried out on a Micromeritics ASAP 2020 instrument. UV-Vis diffuse reflectance spectra (UV-Vis DRS) were tested on a HITCHI UH-4150 spectrophotometer with $BaSO_4$ as the reference. X-ray photoelectron spectroscopy (XPS) were measured on Thermo Fisher Scientific ESCALAB 250 Xi spectrometer. Hydrogen temperature-programmed reduction (H_2-TPR) was conducted on a chemical adsorption analyzer (TP-5080-D) equipped with a thermal conductivity detector (TCD). Ethyl acetate temperature-programmed desorption (Ethyl acetate-TPD) experiments were conducted on a chemical adsorption analyzer (Autochem II 2920, Micromeritics) and a mass spectrometer (OmniStar GSD320). Electrochemical tests were carried out by a Metrohm Autolab PGSTAT204 electrochemical station in a typical three-electrode mode. In situ diffuse reflectance Fourier transform infrared spectroscopic (in situ DRIFTS) experiments were determined on a Bruker Tensor II spectrometer with a liquid nitrogen-cooling MCT detector. An electron paramagnetic resonance (ESR) spectrometer (EMXPlus-6/1, Bruker) was used for the measurement of the EPR signals of photoinduced radicals.

2.5. Catalytic performance

Photothermal catalytic oxidation reactions were carried out in a fixed-bed quartz tubular reactor and the catalyst can be irradiated by a 300 W Xe lamp (Beijing Perfectlight) equipped with a UV-Vis-IR flter (λ = 320–2500 nm) through a small window on the one side of the furnace. The light intensity was measured at the same position to ensure that the error of the light intensity before and after the experiment was less than 5%. In the absence of additional heat supply, the temperature of the catalyst surface was 74 °C under the irradiation of 300 mW•cm^{-2}. Hence, the starting temperature of the photothermal catalytic experiment was 80 °C. When the required temperature of the system was higher than 80 °C, additional heating was performed by setting the temperature controller of furnace. The temperature of the catalyst surface measured by thermocouples was the sum of the temperature induced by the light and the additional heat supply.

The reactant mixture stream was consisted of 200 ppm ethyl acetate + 20 vol% O_2 + N_2 (balance), with a total flow of 16.7 mL/min and a space velocity (SV) of ca. 20,000 mL/(g h). The 200 ppm ethyl acetate was generated through a bottle containing pure ethyl acetate that was chilled in an ice-water isothermal bath at 6 °C. The surface temperature of sample was detected by the thermocouple. Before the test, the sample was treated in O_2 (20 mL/min) at 250 °C for 1 h. The photothermal catalytic stability and the effect of H_2O (5 vol%) or CO_2 (10 vol%) on the 0.26 Pd/3.2 N-TiO_2 catalyst were also investigated. Reactants and products were analyzed online by gas chromatography (GC-2014 C, Shimadzu) equipped with a flame ionization detector (FID), using a stabilwax@ -DA column (30 m in length) for ethyl acetate separation. The ethyl acetate conversion was calculated using the following equation: ethyl acetate conversion (%) = 100 × ([ethyl acetate]$_{inlet}$−[ethyl acetate]$_{outlet}$)/[ethyl acetate]$_{inlet}$, where the [ethyl acetate]$_{inlet}$ and [ethyl acetate]$_{outlet}$ are the inlet and outlet ethyl acetate concentrations in the feed stream, respectively.

3. Results and discussion

3.1. Crystal phase composition, pore structure, and morphology

The PXRD patterns of TiO_2-500, 3.2 N-TiO_2-500, and 0.26 Pd/3.2-TiO_2-500 (abbreviated as TiO_2, 3.2 N-TiO_2, and 0.26 Pd/3.2-TiO_2) are depicted in Fig. 1 A. The as-prepared samples possessed anatase/rutile mixed phase of TiO_2. Compared with TiO_2, the introduction of N and Pd had little effect on the diffraction peak positions and crystal planes composition, while the diffraction peak intensity of the (110) crystal
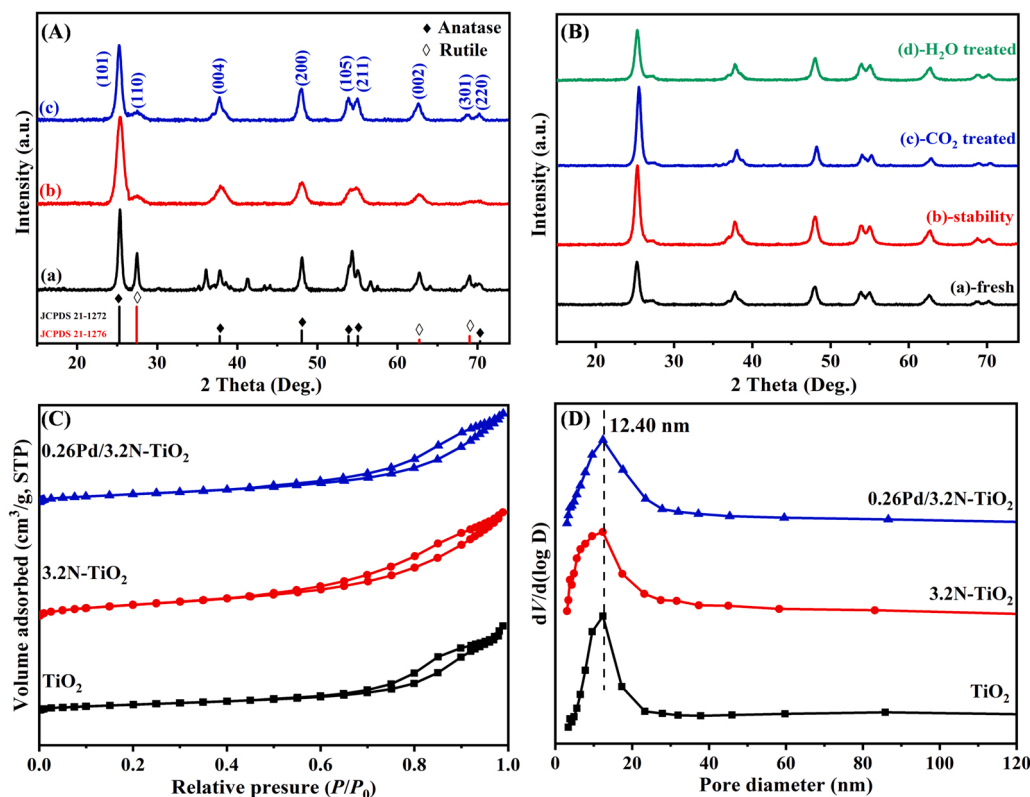
Fig. 1. (A) PXRD patterns of (a) TiO_2, (b) 3.2 N-TiO_2, and (c) 0.26 Pd/3.2 N-TiO_2; (B) PXRD patterns of fresh and used 0.26 Pd/3.2 N-TiO_2; (C) Nitrogen adsorption-desorption isotherms and (D) pore-size distributions of (a) TiO_2, (b) 3.2 N-TiO_2, and (c) 0.26 Pd/3.2 N-TiO_2.

plane decreased, due to the presence of N species might influence the phase transformation between anatase and rutile TiO_2 [24]. The principal peaks located at 25.3°, 37.8°, 48.0°, 53.9°, 55.1°, and 70.3°, could be ascribed to the (101), (004), (200), (105), (211), and (220) crystal planes of anatase TiO_2 (JCPDS 21–1272), respectively. The diffraction peak at 27.4°, 62.7°, and 69.0°, could be due to the (110), (002), and (301) crystal planes of rutile TiO_2 (JCPDS 21–1276), respectively. The diffraction peaks due to the Pd species were not detected, probably due to the low loading of 0.26 Pd/3.2-TiO_2. In addition, the corresponding crystalline grain size, obtained by the Debye-Scherrer formula, of TiO_2, 3.2 N-TiO_2, and 0.26 Pd/3.2-TiO_2 were 23.2, 11.9, and 11.9 nm (Table 1). The introduction of melamine made the grain size smaller, which may be related to the N doping. The smaller crystalline grain sizes of the support could benefit the contact between the catalyst and the reactants, and then improve the catalytic performance.

The mesoporous structure of as-prepared samples could be confirmed by the N_2 adsorption–desorption isotherms in Fig. 1 C. All the

Table 1
Crystalline size, BET surface area, pore diameter, and pore volume of the as-prepared samples.

Sample	Crystalline grain size[a] (nm)	BET surface area[b] (m^2/g)	Pore diameter[b] (nm)	Pore volume[b] (cm^3/g)	Surface O_A/O_L molar ratio
TiO_2	23.2	58.8	12.4	0.22	0.10
3.2 N-TiO_2	11.9	104.7	12.4	0.27	0.11
0.26 Pd/3.2 N-TiO_2	11.9	73.1	12.4	0.23	0.11

[a] Data were determined based on the XRD results according to the Debye-Scherrer equation;
[b] Data were determined by the BET method;

samples displayed IV-typed isotherms with a H1-typed hysteresis loop in the relative pressure range of 0.6–1.0, indicating the successful preparation of mesoporous sample [25]. The average pore diameter of the as-prepared samples was 12.40 nm (Fig. 1D), and the pore volume was in the range of 0.22–0.27 $cm^3 \cdot g^{-1}$. The surface areas of TiO_2, 3.2 N-TiO_2, and 0.26 Pd/3.2 N-TiO_2 were 58.8, 104.7, and 73.1 $m^2 \cdot g^{-1}$, respectively. The introduction of N increased the surface area of the sample, due to the smaller crystalline grain size (as shown by the XRD results). The surface area decreased after loading Pd NPs, due to the coverage of Pd NPs. The abundant pore structure and large surface area were conducive to the rapid migration of pollutants, and then the enhancement of photothermal catalytic activity.

The morphologies and elemental composition of the present samples could be seen from the TEM images and elemental analysis. The original MIL-125 showed a disk-like morphology (Fig. 2A), and after calcination at high temperature, small crystalline grains could be observed (Fig. 2B). After calcination with melamine, as shown in Fig. 2C and D, 3.2 N-TiO_2 and 0.26 Pd/3.2-TiO_2 basically kept the original morphology of MIL-125, while the disk-like structure consists of numerous smaller grains with a size of 10–15 nm, which was in accordance with the XRD results. Fig. 2E showed the existence of the (101) plane of TiO_2 (anatase), (110) plane of TiO_2 (rutile), and the (200) plane of Pd, indicating that 0.26 Pd/3.2-TiO_2 was composed of anatase/rutile mixed phases, and Pd NPs were successfully loaded on the support. This result could also be confirmed by Fig. 2F-K, where the Pd NPs were uniformly dispersed on the support, and the size of the Pd NPs was in the range of 25–35 nm.

3.2. Catalytic performance

The composition of rutile and anatase in TiO_2 would affect the catalytic oxidation performance. The calcination temperature will directly affect the crystal phase composition of TiO_2 [26]. Therefore, the photothermal catalytic oxidation of ethyl acetate over TiO_2 calcined at 500,
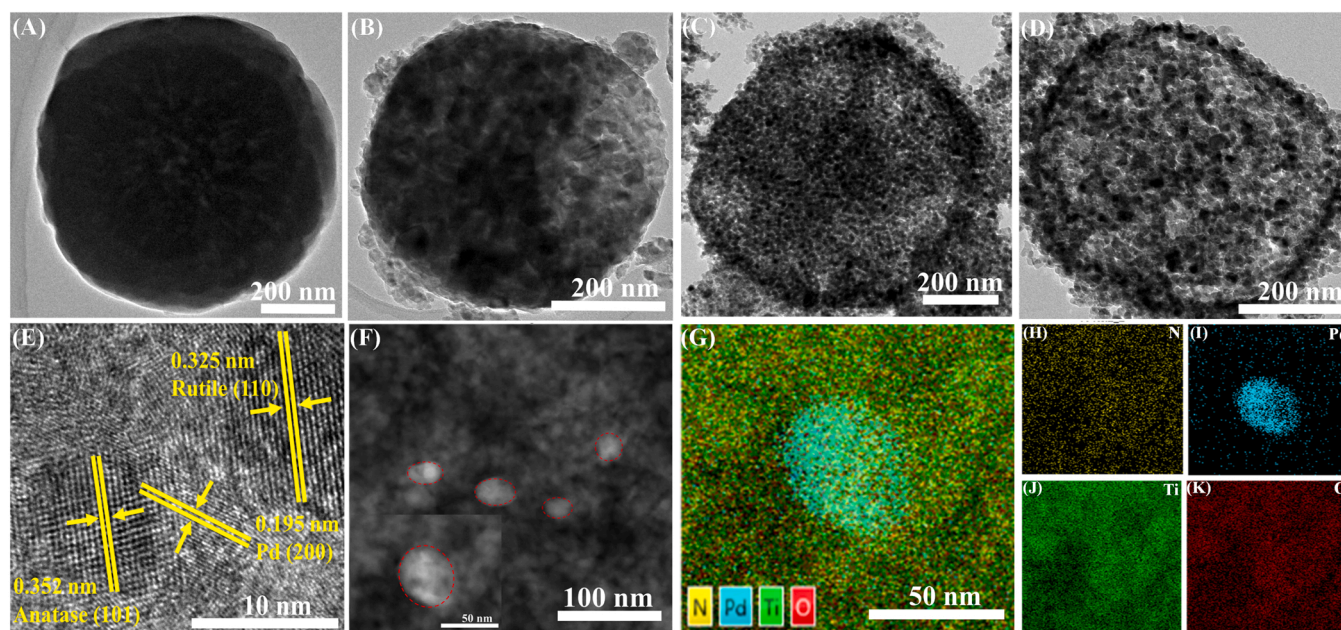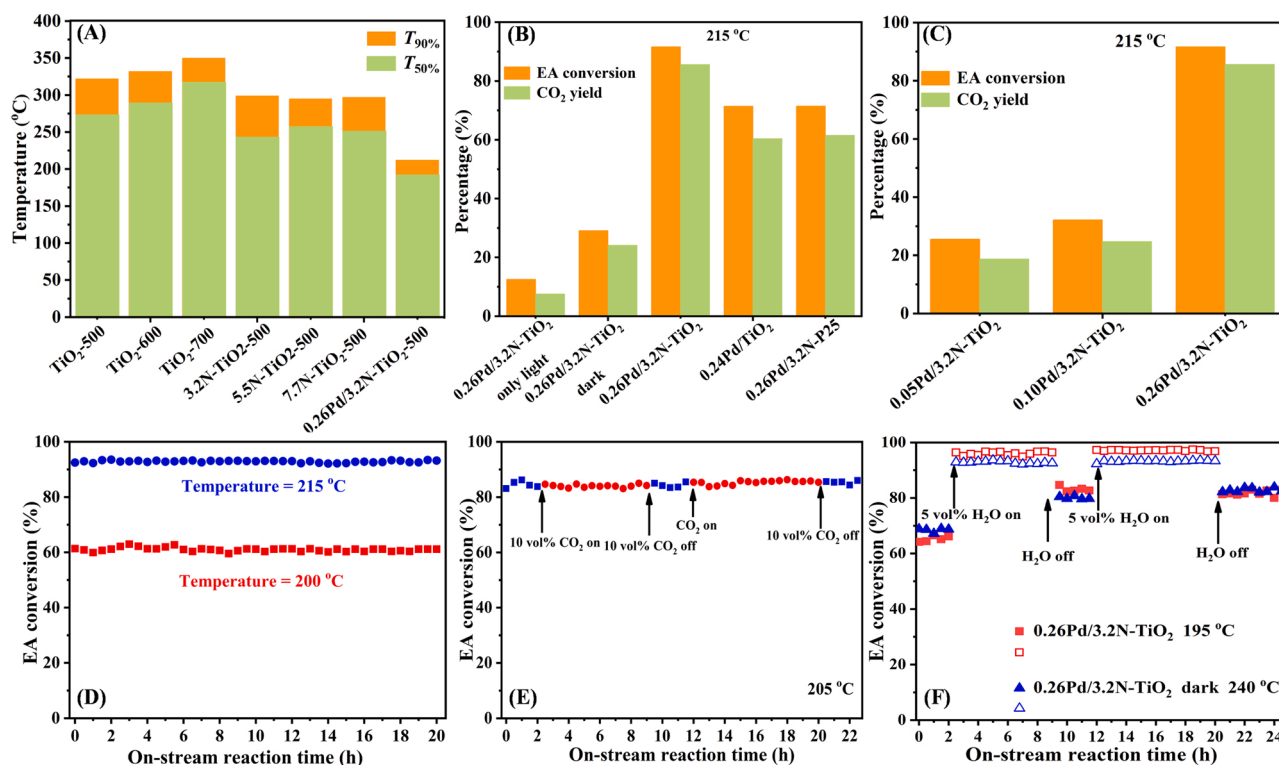
NPs were the most active sites for ethyl acetate oxidation.

To demonstrate the photo-thermo synergistic effect, the catalytic activity of 0.26 Pd/3.2 N-TiO$_2$ for ethyl acetate was investigated under the conditions of only light, only heat and the coexistence of light and heat, respectively. In Fig. 3B, under the condition of only light irradiation, the catalytic activity of 0.26 Pd/3.2 N-TiO$_2$ was very poor, and the ethyl acetate conversion and CO$_2$ yield were only 12.5% and 7.5%, respectively. At the same time, the temperature of the catalyst measured by a thermocouple was 74 °C, which ruled out the possibility of light-driven thermocatalysis of ethyl acetate. The conversion and CO$_2$ yield were slightly improved (29.1% and 24.1%) in the absence of light, but far lower than that under the coexistence of light and heating (91.6% and 85.6%). It could be indicated that the high catalytic activity of 0.26 Pd/3.2 N-TiO$_2$ towards ethyl acetate was the result of photo-thermo synergy. It could be seen from Fig. S1 that over 0.26 Pd/3.2 N-TiO$_2$ at the same temperature, the conversion rate of ethyl acetate under the coexistence of light and heating was always higher than that only under heating, further confirming the high photothermal synergistic catalytic oxidation performance for ethyl acetate removal. Furthermore, the conversion of ethyl acetate over 0.24 Pd/TiO$_2$-500 (noted as 0.24 Pd/TiO$_2$) was also lower than that over 0.26 Pd/3.2 N-TiO$_2$. Combined with the above results, it could be seen that the simultaneous introduction of N and Pd was beneficial to improve the catalytic activity towards ethyl acetate. Moreover, the performance of 0.26 Pd/3.2 N-TiO$_2$ was also higher than that of 0.26 Pd/3.2 N-P25–500 (noted as 0.26 Pd/3.2 N-P25). As shown in Fig. S2, 0.26 Pd/3.2 N-P25 displayed I-typed isotherm, suggesting presence of micropores in 0.26 Pd/3.2 N-P25. In addition, the average pore size of the catalyst was 1.0 nm. The 0.26 Pd/3.2 N-TiO$_2$ catalyst derived from MIL-125(Ti) had abundant pore structure and large specific surface area of 73.1 m$^2 \cdot$g^{-1}, which were beneficial to the adsorption of pollutants, therefore 0.26 Pd/3.2 N-TiO$_2$ exhibited better photothermal catalytic oxidation activity than 0.26 Pd/3.2 N-P25. It could be seen from Fig. 3 C that the photothermal catalytic activity towards ethyl acetate was improved gradually with the increase of Pd content. Considering of saving resources and reducing costs, this work did not continue to increase the loading of Pd. For better compare the catalytic performance of each catalyst, specific reaction rates at 150 °C were estimated, as listed in Table 2. The specific reaction rates (2.66 μmol/(g$_{Noble\ mental}$ s)) and 0.69 × 10^{-2} μmol/(g$_{Cat}$ s)) over 0.26 Pd/3.2 N-TiO$_2$ were higher than that over 0.24 Pd/TiO$_2$ (2.28 μmol/(g$_{Noble\ mental}$ s) and 0.55 × 10^{-2} μmol/(g$_{Cat}$ s)), 0.26 Pd/3.2 N-P25 (2.49 μmol/(g$_{Noble\ mental}$ s) and 0.57 × 10^{-2} μmol/(g$_{Cat}$ s)), and 0.26 Pd/3.2 N-TiO$_2$ under dark (0.96 μmol/(g$_{Noble\ mental}$ s) and 0.25 × 10^{-2} μmol/(g$_{Cat}$ s)). This corresponds to the alteration trend of catalytic activity of catalysts. In addition, we also compared the catalytic activity of 0.26 Pd/3.2 N-TiO$_2$ with other supported noble metal catalysts reported in previous work (listed in Table 3). Due to the inconsistent reaction conditions such as concentration, space velocity and reaction mode, it was difficult to compare the catalytic performance. Although the catalytic performance of 0.26 Pd/3.2 N-TiO$_2$ was lower than that of noble metal catalysts with higher loadings, it was still better or comparable to that of catalysts with similar loading. Considering that photothermal synergistic catalysis

could greatly reduce CO$_2$ emissions and energy consumption from heat supply and 0.26 Pd/3.2 N-TiO$_2$ derived from MIL-125(Ti) enhance the light absorption capacity, promote the charge separation and the adsorption capacity of ethyl acetate, resulting in a high photothermal catalytic oxidation activity, the photothermal catalytic system reported in this work was still very meaningful.

The stability of the catalyst had a great influence on its practical application, so the catalytic oxidation stability test was carried out at 200 °C ($\approx T_{60\%}$) and 215 °C ($\approx T_{90\%}$), respectively. It could be seen from Fig. 3D that the conversion of ethyl acetate had no significant change within 20 h, indicating that 0.26 Pd/3.2 N-TiO$_2$ had the potential to be used for a long time. In addition, industrial exhaust emissions may also contain H$_2$O and CO$_2$, which may compete with VOCs for adsorption, resulting in a decrease in the catalytic activity. Therefore, the influence of water vapor and CO$_2$ on photo-thermo catalytic performance of 0.26 Pd/3.2 N-TiO$_2$ were also investigated. In Fig. 3E, addition of CO$_2$ had negligible effect on the conversion of ethyl acetate, which could be kept stable at around 80%. This may be due to the weaker adsorption of CO$_2$ than that of ethyl acetate. Unexpectedly, as exhibited in Fig. 3F, the conversion of ethyl acetate increased from about 60% to about 95% after the introduction of H$_2$O. After cutting off the water vapor, the conversion dropped and remained around 80%. This phenomenon could also be observed in thermocatalysis, indicating that it was not caused by light irradiation. According to our previous study, the oxygen in the water would exchange with the adsorbed oxygen or lattice oxygen of the catalyst, and generate new OOH species, which could be decomposed into·OH, confirmed by the isotopic H$_2^{18}$O and D$_2$O analysis method [40]. The·OH could further react with the adsorbed oxygen, generating more active oxygen species (O$_2^-$ and O$^-$) [41]. Therefore, the improved catalytic activity after the introduction of water was reasonable. The XRD and XPS spectra of 0.26 Pd/3.2 N-TiO$_2$ after stability and H2O/CO2 resistance tests were demonstrated in Figs. 1B and S3. Obviously, the crystal phase structure, surface element compositions, and metal chemical states of 0.26 Pd/3.2 N-TiO$_2$ before and after the reaction did not change. The above results indicated that 0.26 Pd/3.2 N-TiO$_2$ exhibited outstanding stability and practical application potential.

3.3. Surface property

The surface element composition, oxygen species and metal oxidation states of the catalyst could be obtained by XPS. The peaks at 458.4 eV and 464.0 eV (Fig. 4A) could belong to Ti 2p$_{1/2}$ and Ti 2p$_{3/2}$, which demonstrates that Ti exists as Ti^{4+} in catalysts [42]. Each N 1 s spectrum could be decomposed into four components at BE = 397.1, 398.5, 399.3 eV and 400.9 eV (Fig. 4B), which were ascribed to N-Ti-N, N-Ti-O, Ti-O-N and Ti-N-O, respectively, indicated N was partially doped into the lattice of TiO$_2$ [43–46]. Three peaks at 529.6 eV, 531.0 eV and 532.2 eV (Fig. 4 C) could reveal the presence of the surface lattice oxygen (O$_L$), adsorbed oxygen (O$_A$), and surface adsorbed water species [47,48]. The O$_A$/O$_L$ molar ratio of TiO$_2$, 3.2 N-TiO$_2$ and 0.26 Pd/3.2 N-TiO$_2$ were about the same (listed in the Table 1), suggested O$_A$/O$_L$ was not an important factor affecting the catalytic activity in this study. The Pd 3d spectrum was presented in Fig. 4D, in which the 335.7 and 340.7 eV peaks corresponded to Pd^0 species, and the ones at 338.4 and 343.7 eV corresponded to Pd$^{\mathcal{E}+}$ species ($2 < \mathcal{E} \le 4$) [49,50].

3.4. Low-temperature reducibility and toluene adsorption ability

According to previous studies [51], reducibility was an important factor affecting the thermocatalytic performance of catalysts. As shown in Fig. 5 A, each catalysts exhibited two peaks between 350 and 400 °C and 550–600 °C, the former could be attributed to the reduction of surface lattice oxygen and the latter was related to the reduction of Ti^{4+} to Ti^{3+} [52]. The strong interaction between the noble metal and the support made the reduction peak of 0.26 Pd/3.2 N-TiO$_2$ shift to low temperature, which improved its reducibility and contributed to the

Table 2
Catalytic activities and ethyl acetate reaction rates at 150 °C of the catalysts.

Catalyst	Catalytic activity		Ethyl acetate conversion at 150 °C	
	$T_{50\%}$ (°C)	$T_{90\%}$ (°C)	Reaction rate (μmol/(g$_{Noble\ metal}$ s))	Reaction rate (× 10^{-2} μmol/(g$_{Cat}$ s))
0.26 Pd/3.2 N-TiO$_2$ only light	–	–	–	–
0.26 Pd/3.2 N-TiO$_2$ dark	230	249	0.96	0.25
0.26 Pd/3.2 N-TiO$_2$	192	212	2.66	0.69
0.24 Pd/TiO$_2$	204	228	2.28	0.55
0.26 Pd/3.2 N-P25	200	229	2.49	0.57

Table 3

Catalytic performance for ethyl acetate oxidation over various supported noble metal catalysts.

Catalyst	ethyl acetate concentration (ppm)	Space velocity	$T_{90\%}$ (°C)	Reaction mode	Ref.
1Ru–5Cu/TiO$_2$	500	60,000 mL g^{-1} h^{-1}	208	Thermocatalysis	[28]
1.0 wt% Ru/SnO$_2$	1000	10,000 mL g^{-1} h^{-1}	210	Thermocatalysis	[29]
2.0 wt% Pt/Co$_3$O$_4$-CeO$_2$	900	30,000 mL g^{-1} h^{-1}	210	Thermocatalysis	[30]
0.84Au/CeO$_2$	466	53,050 h^{-1}	240	Thermocatalysis	[31]
0.91Au$_{0.48}$Pd/α-MnO$_2$	1000	40,000 mL g^{-1} h^{-1}	187	Thermocatalysis	[32]
0.5 Pd/Cr$_2$O$_3$-ZrO$_2$	1500	20,000 h^{-1}	190	Thermocatalysis	[33]
0.5Pt/CeO$_2$	5000	1000 h^{-1}	246	Thermocatalysis	[34]
0.5 Pd/Al$_2$O$_3$	1000	50,000 h^{-1}	277	Thermocatalysis	[35]
0.91 Pd/CeO$_2$	1000	60,000 mL g^{-1} h^{-1}	180	Thermocatalysis	[36]
1.0 wt% Ag/LaCoO$_3$	500	60,000 mL g^{-1} h^{-1}	190	Thermocatalysis	[37]
1.0 wt% Ru/CeO$_2$	1000	15,000 h^{-1}	180	Thermocatalysis	[38]
0.28 Pd/ZSM-5	1033	26,000 h^{-1}	240	Thermocatalysis	[39]
0.26 Pd/3.2 N-TiO$_2$	200	20,000 mL g^{-1} h^{-1}	212	Photo-thermo catalysis	This work
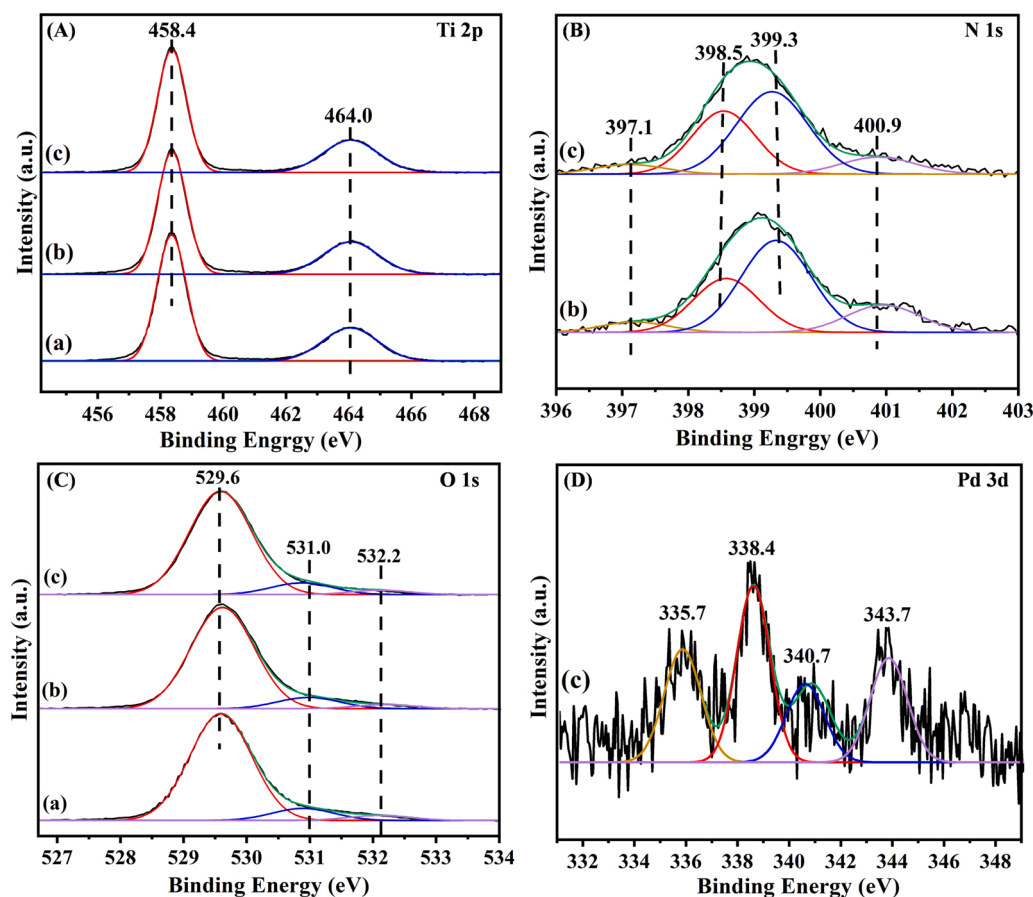
Fig. 4. (A) Ti 2p, (B) N 1 s, (C) O 1 s and (D) Pd 3d XPS spectra of (a) TiO$_2$, (b) 3.2 N-TiO$_2$, and (c) 0.26 Pd/3.2 N-TiO$_2$.

enhancement of photo-thermo catalytic activity [53]. This could also be confirmed by the quantitative analysis of the H$_2$-TPR reduction peak to obtain the H$_2$ consumption of the catalysts, which below 600 °C decreased in the order of 9.00×10^{-2} mmol/g$_{cat}$ (0.26 Pd/3.2 N-TiO$_2$) $> 6.52 \times 10^{-2}$ mmol/g$_{cat}$ (3.2 N-TiO$_2$) $> 1.07 \times 10^{-2}$ mmol/g$_{cat}$ (TiO$_2$).

In addition to the low-temperature reducibility, the adsorption capacity for VOCs also influenced the catalytic performance of the catalyst [54]. The adsorption of ethyl acetate on the catalysts was investigated by ethyl acetate-TPD technique, shown in Fig. 5B-D. All catalysts possessed two desorption peaks of ethyl acetate between 50 and 900 °C, which might be due to the desorption peaks of physically or weakly chemisorbed ethyl acetate. The ethyl acetate and CO$_2$ desorption peak intensities over 0.26 Pd/3.2 N-TiO$_2$ were higher than that over TiO$_2$ and 3.2 N-TiO$_2$, which indicated that the greater adsorption capacity of ethyl

acetate on 0.26 Pd/3.2 N-TiO$_2$. This was mainly attributed to the strong interaction between Pd and N-TiO$_2$ [49,51]. In addition, the rich pore structure and high specific surface area were also beneficial to improve the adsorption capacity [55]. Considering the importance of the adsorption capacity of the reactants, the excellent photo-thermo catalytic oxidation performance of 0.26 Pd/3.2 N-TiO$_2$ was related to the larger adsorption of ethyl acetate.

3.5. Optical properties

In photocatalysis, the light absorption and carrier separation ability of the catalyst were very significant for the capability of the catalyst [56, 57]. Optical properties of the catalysts were examined by the UV-Vis-IR spectroscopy (Fig. 6 A). TiO$_2$, 3.2 N-TiO$_2$ and 0.26 Pd/3.2 N-TiO$_2$ had
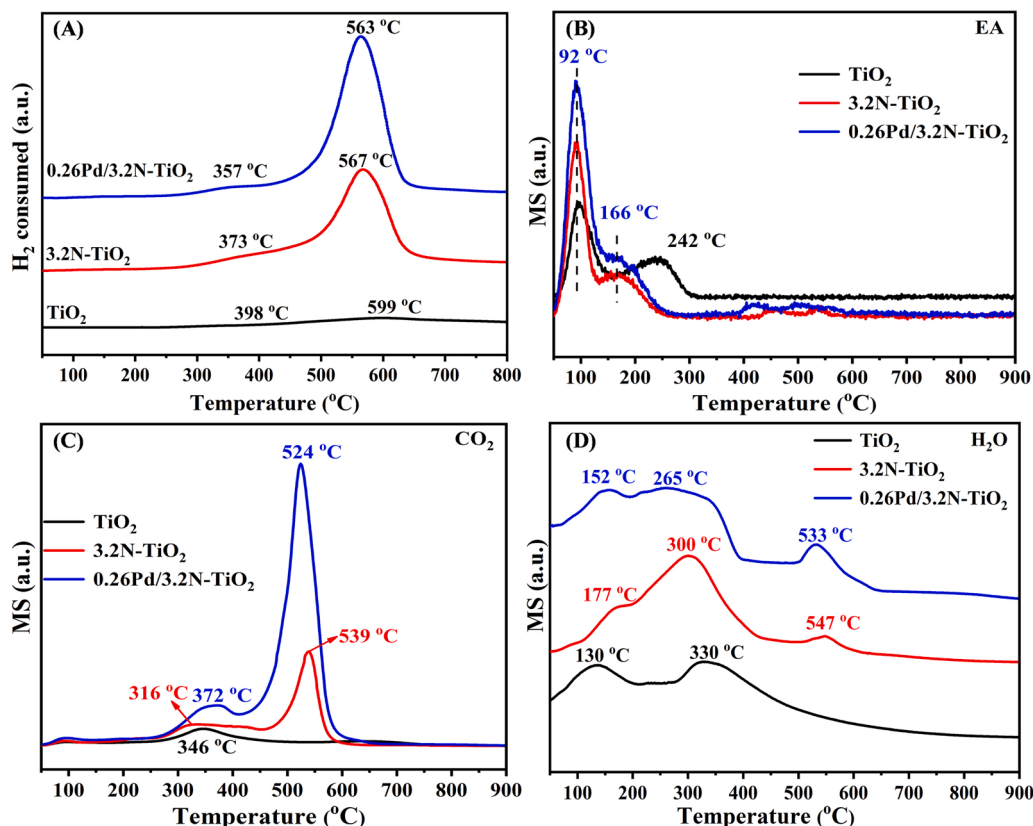
Fig. 5. (A) H_2-TPR profiles and (B) ethyl acetate, (C) CO_2, (D) H_2O desorption in the ethyl acetate-TPD profiles of TiO_2, 3.2 N-TiO_2 and 0.26 Pd/3.2 N-TiO_2.
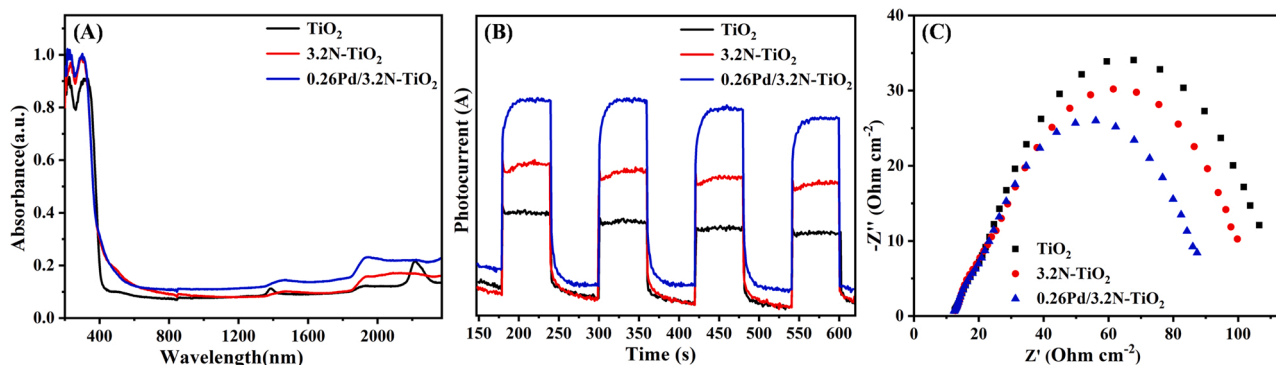

Fig. 6. (A) UV-Vis-IR spectra, (B) Amperometric current-time curves and (C) EIS Nyquist plots of TiO_2, 3.2 N-TiO_2 and 0.26 Pd/3.2 N-TiO_2 under light irradiation.

similar absorption behaviors in the whole solar spectral range (200–2400 nm), but 0.26 Pd/3.2 N-TiO_2 presented stronger absorption. As expected, 3.2 N-TiO_2 and 0.26 Pd/3.2 N-TiO_2 exhibited strong optical absorption in the range of 400–700 nm, which was missing in the spectrum of TiO_2. It showed that the introduction of N made the catalyst have higher solar light utilization efficiency, which might help improve the catalytic performance [58]. In addition, the light absorption of 0.26 Pd/3.2 N-TiO_2 was similar to that of 3.2 N-TiO_2, indicating that there was no plasmonic effect due to the presence of Pd NPs [10]. In order to explore the photo-generated carrier separation ability, the amperometric current-time curves and EIS Nyquist plots of the catalysts were determined. Obviously, 0.26 Pd/3.2 N-TiO_2 exhibited higher photocurrent response to each illumination cycles than those of TiO_2 and 3.2 N-TiO_2 (Fig. 6B) and a small diameter of arc radius (Fig. 6 C), indicating that Pd NPs could capture the photo-generated electrons and then hinder charge recombination. Based on the above results, it was

reasonable to believe that the better photo-thermo catalytic oxidation activity of 0.26 Pd/3.2 N-TiO_2 also benefited from the excellent light absorption ability and electron-hole separation ability.

3.6. Possible reaction pathway and photo-thermo catalytic mechanism

In order to determine the products that may be generated during the photo-thermo catalytic oxidation, the TD-GC/MS technique was employed (Figs. 7A and S4). At low temperature, only ethanol was detected, and as the temperature increased, ethanol gradually disappeared and acetic acid began to appear. When the ethyl acetate conversion rose to 90%, only acetic acid was detected. To further understand the possible reaction pathways, *in situ* DRIFTS characterizations were performed under different conditions. Firstly, the adsorption of ethyl acetate on 0.26 Pd/3.2 N-TiO_2 with various time was investigated at 80 °C (Fig. 7B). The bands at 1770–1720 cm^{-1},
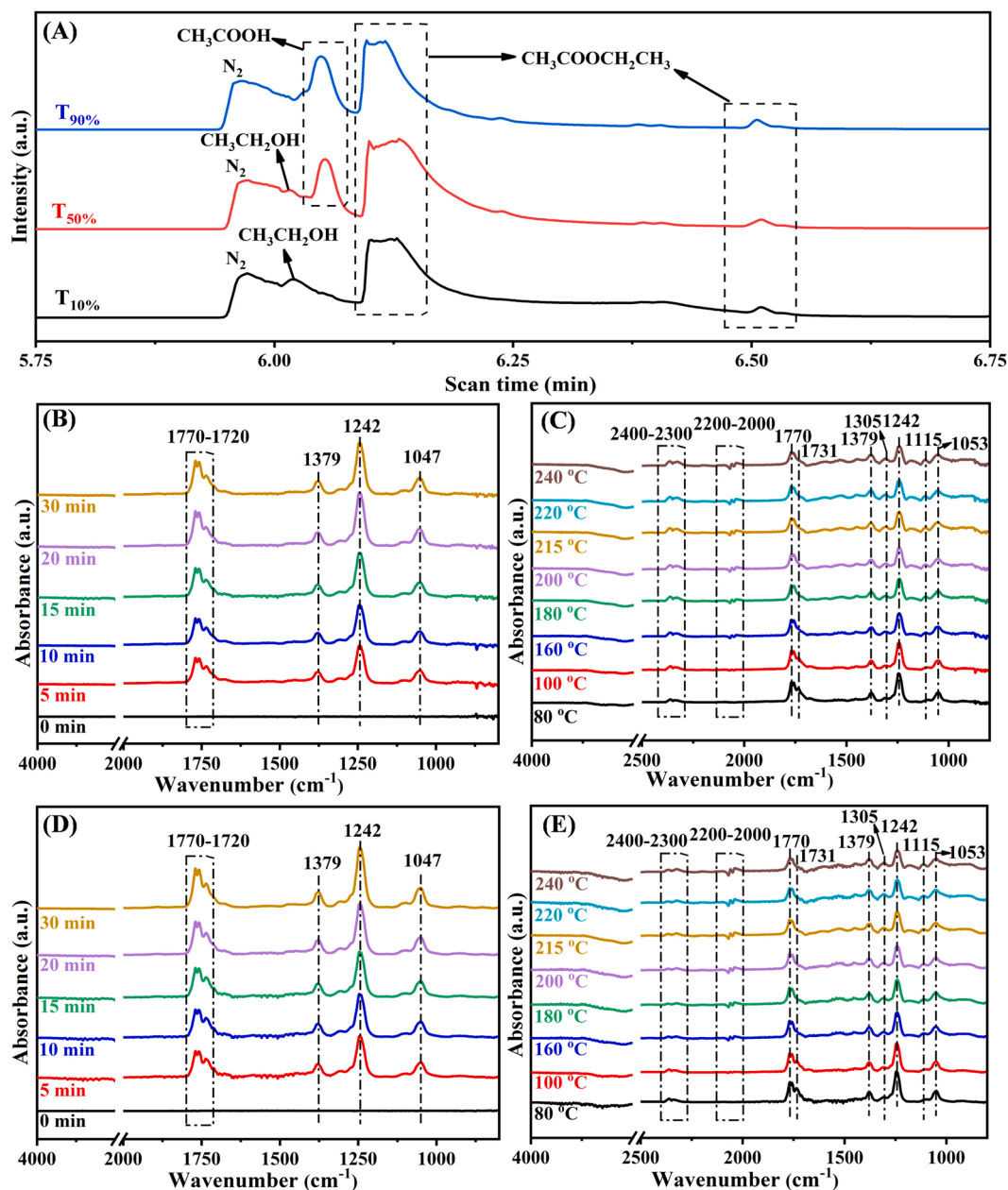
Fig. 7. (A) GC-MS spectra of ethyl acetate catalytic oxidation over 0.26 Pd/3.2 N-TiO₂; *In situ* DRIFTS spectra of ethyl acetate adsorption at different time under the condition of (B) coexistence of light and heat and (D) absence of light; In situ DRIFTS spectra of ethyl acetate catalytic at different temperatures over 0.26 Pd/3.2 N-TiO₂ under the condition of (C) coexistence of light and heat and (E) absence of light.

1379 cm^{-1}, 1242 cm^{-1} and 1047 cm^{-1} were ascribed to the stretching frequency of C=O, CH₃ bend, the C-O stretching in the O=C-O group and the stretching vibration of C-O-C from ethyl acetate, respectively [59,60]. It could be seen that the absorption band intensity of ethyl acetate increased with the time, indicating that the addition of adsorption amount. Moreover, the ethyl acetate in a (200 ppm ethyl acetate +20 vol% O_2 + N_2 (balance)) flow at different temperatures were also carried out (Fig. 7 C). The bands at 2400–2300 cm^{-1} were the stretching vibrations of C-O bonds from CO_2, and the bands at 2200–2000 cm^{-1} were the C-O stretching of CO. The band at 1770 cm^{-1}, 1379 cm^{-1} and 1305 cm^{-1}, 1242 cm^{-1}, 1115 cm^{-1} and 1053 cm^{-1} could be ascribed to the C=O stretching of acetic acid, the overlapping COO^- symmetric stretching vibrations and CH₃ stretching vibration of acetate and the C-C stretching vibrations and C-O stretching of ethanol, respectively [28, 61]. Combined the above results, the approximate catalytic oxidation process could be obtained. Due to the small bond dissociation energy,

the initial reaction pathway of ethyl acetate was the cleavage of C-C and C-O to form CH₃COO* , CH₃CH₂O* and CH₃CO* groups. Further intermediates such as acetic acid, ethanol and acetaldehyde were produced and eventually oxidized to CO_2 and H_2O [62,63]. It had been reported that the introduction of light could accelerate the formation of intermediates or/and change the reaction pathway, thus promote the catalytic oxidation process [64,65]. In order to explore whether there was a similar phenomenon in this system, the *in situ* DRIFTS in the absence of light were also carried out (Fig. 7D and E). It could be found that the introduction of light had little effect on the pathway and reaction intermediates of the catalytic oxidation. Moreover, the *in situ* DRIFTS under the coexistence of light and heating (Fig. S5A) and absence of light (Fig. S5B) at 215 °C were conducted, when the conversion rate of ethyl acetate had significant difference between the thermocatalytic and photothermal synergistic catalytic oxidation. The intermediate products of the catalytic oxidation of ethyl acetate over

0.26 Pd/3.2 N-TiO$_2$ did not change at different times at 215 °C. Hence, we speculated that the conversion rate of ethyl acetate exhibited significant difference was not due to the change of the reaction pathway, and there might be other reasons for the enhanced photothermal synergistic activity.

To explore the reaction mechanism, the Mott-Schottky measurement was used to determine the conduction band (CB) values of 0.26 Pd/3.2 N-TiO$_2$ (Fig. 8A). It was found that the flat-band potential (E_{FB}) of 0.26 Pd/3.2 N-TiO$_2$ was ca. − 0.70 eV versus the Ag/AgCl electrode. According to literature reports, the E_{FB} is 0.2 eV more positive than the E_{CB} for n-type semiconductor [66]. Therefore, the CB of 0.26 Pd/3.2 N-TiO$_2$ was ca. −0.50 eV versus normal hydrogen electrode (NHE) at pH 7.3. According to the formula $E_{CB} = E_{VB} - E_g$ (Fig. 8B), the valence band (VB) value of 0.26 Pd/3.2 N-TiO$_2$ was calculated as 2.58 eV versus NHE. Because the E_{CB} was higher than the standard potential of O$_2$/·O$_2^-$ (–0.33 eV vs. NHE) and the E_{VB} was lower than that (2.40 eV vs. NHE) of the OH$^-$/·OH pair, ·O$_2^-$ and ·OH could be generated over the CB and VB during the catalytic oxidation process theoretically.

To better understand the enhanced photothermal synergistic catalytic activity for ethyl acetate oxidation of 0.26 Pd/3.2 N-TiO$_2$, radicals generated during oxidation were evaluated. As shown in Fig. 8C and D, the ESR experiment with DMPO technique was used to detect the formed ·O$_2^-$ and ·OH over the 0.26 Pd/3.2 N-TiO$_2$. Obviously, no signals could be observed in the absence of light. When upon the illumination for 10 min, the signals of ·O$_2^-$ and ·OH were found clearly, indicating that in the process of photothermal synergistic catalytic oxidation, ·O$_2^-$ could be generated and lead to the efficient oxidation of ethyl acetate. Since no water was added to the actual reaction process, the signals of ·OH detected by ESR could indicate that 0.26 Pd/3.2 N-TiO$_2$ had the ability to use the water generated by the reaction to react with h$^+$ to generate ·OH during the photothermal catalytic oxidation process. The ·OH species were also participated in the catalytic reaction of ethyl acetate

[59]. In addition, this phenomenon could also explain that the improved catalytic activity of ethyl acetate after adding water (Fig. 3 F) may be related to the generation of ·OH, which were then converted into more reactive oxygen species. Besides, the similar phenomenon was also observed on TiO$_2$ and 3.2 N-TiO$_2$. The signal of •O$_2^-$ and •OH could be detected only under the light condition. However, the quantitative analysis (Table 4) of •O$_2^-$ and •OH showed that the amount of free radicals decreased in the following order: 0.26 Pd/3.2 N-TiO$_2$ > 3.2 N-TiO$_2$ > TiO$_2$, consistent with the change of photothermal catalytic activity, indicating that •O$_2^-$ and •OH participated in the photothermal synergistic catalytic oxidation reaction.

The possible mechanism of the photothermal synergistic catalytic oxidation of ethyl acetate over 0.26 Pd/3.2 N-TiO$_2$ could be speculated (Fig. 9 A). The thermocatalytic oxidation of VOCs on TiO$_2$ takes place following the Mars-van Krevelen mechanism [67]. For the photo-thermo catalytic oxidation of ethyl acetate over 0.26 Pd/3.2 N-TiO$_2$, the presence of Pd NPs greatly increased the conversion of ethyl acetate, so it was reasonable to believe that the photothermal synergistic catalytic oxidation mainly occurred on the surface of Pd NPs. Due to excellent ability of 0.26 Pd/3.2 N-TiO$_2$ to separate photo-generated carriers, the photo-generated electrons would be transferred from 3.2 N-TiO$_2$ to Pd NPs, and react with the oxygen adsorbed on the surface of Pd NPs to generate reactive oxygen species (·O$_2^-$), which would further react with

Table 4
The number of free radical spins per unit volume of the catalyst under light conditions.

Catalyst	·O$_2^-$ (spins/mm^3)	·OH (spins/mm^3)
TiO$_2$	1.32×10^{13}	1.06×10^{12}
3.2 N-TiO$_2$	1.41×10^{13}	1.36×10^{12}
0.26 Pd/3.2 N-TiO$_2$	1.73×10^{13}	1.98×10^{12}
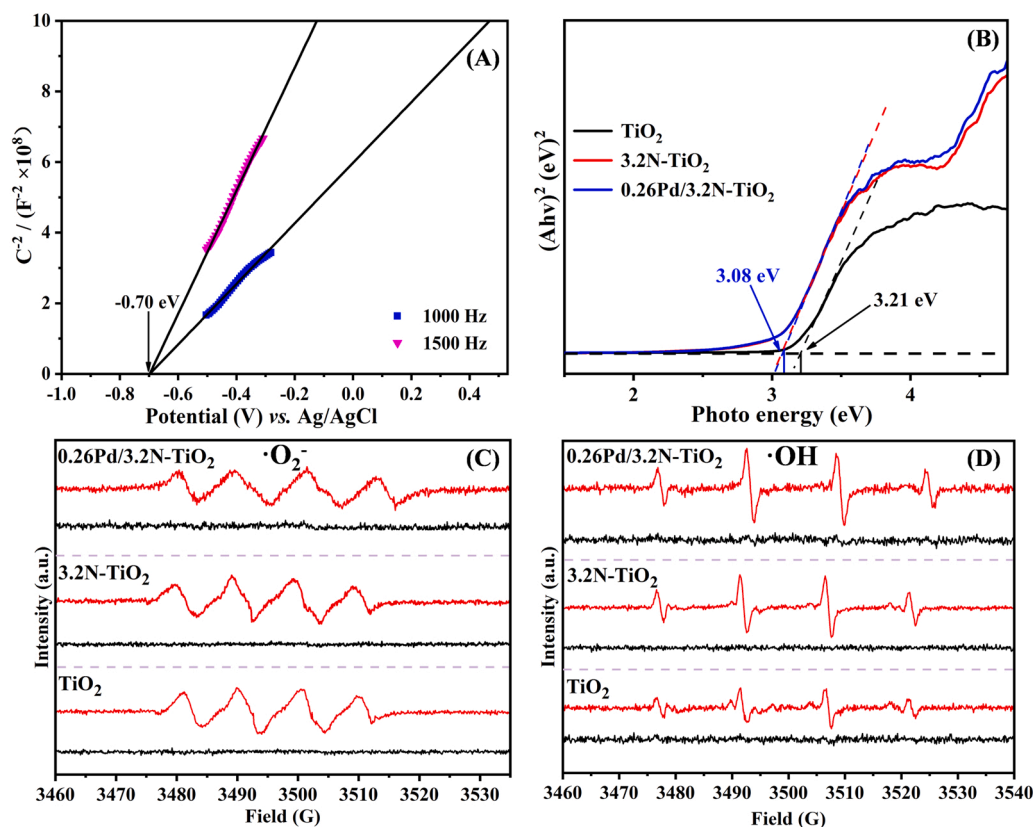
Fig. 8. (A) Mott-Schotty curves of 0.26 Pd/3.2 N-TiO$_2$ at different frequencies; (B) E_g plots of TiO$_2$, 3.2 N-TiO$_2$ and 0.26 Pd/3.2 N-TiO$_2$; (C) and (D) ESR spectra of ·O$_2^-$ and ·OH active radicals on TiO$_2$, 3.2 N-TiO$_2$ and 0.26 Pd/3.2 N-TiO$_2$ (black line: dark; red line: light).
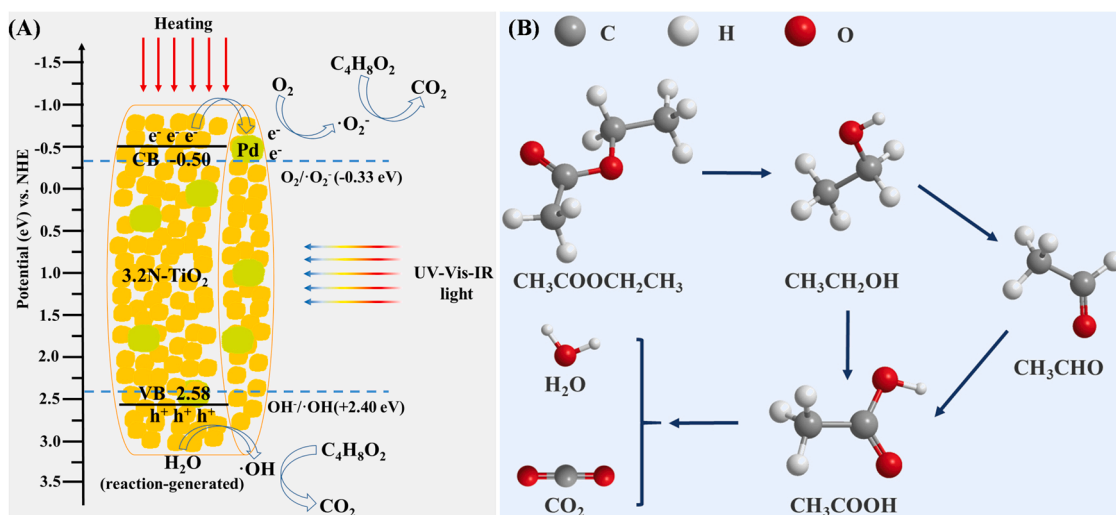
Fig. 9. (A) Proposed reaction mechanisms of photo-thermo catalytic oxidation of ethyl acetate over 0.26 Pd/3.2 N-TiO$_2$; (B) The possible pathway of ethyl acetate oxidation over 0.26 Pd/3.2 N-TiO$_2$.

adjacent ethyl acetate, producing intermediate products such as acetic acid, ethanol and acetaldehyde, and eventually generate CO$_2$ and H$_2$O (Fig. 9B). In addition, the water generated by the reaction could react with holes to generate·OH, the holes and·OH directly participated in the photothermal catalytic. According to the previous work, it could be concluded that appropriate temperature rise was conducive to the rapid transfer of carriers to the active site of the catalyst and desorption or/and conversion of intermediate products from the perspective of thermocatalysis [10]. In conclusion, the high photothermal catalytic performance benefited from the synergistic effect of photothermal.

4. Conclusions

In general, MIL-125 was used to prepare mesoporous disk-like N-TiO$_2$ by a simple ball milling-calcination method. The derived N-TiO$_2$ had smaller grain sizes and larger specific surface areas, which were beneficial to the rapid migration of contaminants and products. Loading Pd NPs greatly enhanced the photothermal catalytic oxidation activity. The better reducibility and larger adsorption capacity of ethyl acetate were one of the reasons for the excellent catalyst activity. 0.26 Pd/ 3.2 N-TiO$_2$ could well inhibit the recombination of photo-generated electrons and holes, under photothermal conditions, photo-generated electrons could react with oxygen to generate more reactive oxygen species. Meanwhile, proper temperature rise was conducive to the rapid migration of carriers, so the improvement of photothermal catalytic (the conversion of ethyl acetate could reach 50% and 90% at 192 °C and 212 °C, respectively) could be attributed to the result of photothermal synergy. Overall, this study developed photothermal synergistic catalytic oxidation method for the removal of ethyl acetate, not only reduce the energy consumption required for thermocatalysis, but also improve the catalytic purification efficiency. The innovation of treatment technology and catalyst provided more possibilities for efficient and energy-saving VOCs removal.

CRediT authorship contribution statement

Xun Wang: Data curation, Investigation, Visualization, Writing – original draft preparation. **Linke Wu:** Methodology, Validation, Software. **Zhiwei Wang:** Instrumental, Data curation. **Ying Feng:** Instrumental, Data curation. **Yuxi Liu:** Investigation. **Hongxing Dai:** Investigation, Data curation. **Zhihua Wang, Jiguang Deng:** Investigation, Data curation. Writing – review & editing, Supervision, Project administration.

Declaration of Competing Interest

The authors declare that they have no known competing financial interests or personal relationships that could have appeared to influence the work reported in this paper.

Data availability

Data will be made available on request.

Appendix A. Supporting information

Supplementary data associated with this article can be found in the online version at doi:10.1016/j.apcatb.2022.122075.

References

[1] C. He, J. Cheng, X. Zhang, M. Douthwaite, S. Pattisson, Z. Hao, Chem. Rev. 119 (2019) 4471–4568.
[2] Y. Dumanoglu, M. Kara, H. Altiok, M. Odabasi, T. Elbir, A. Bayram, Atmos. Environ. 98 (2014) 168–178.
[3] M. Wen, S. Song, W. Zhao, Q. Liu, J. Chen, G. Li, T. An, Environ. Sci.: Nano 8 (2021) 3735–3745.
[4] Y. Yang, Y. Li, Q. Zhang, M. Zeng, S. Wu, L. Lan, X. Zhao, J. Mater. Chem. A 6 (2018) 14195–14206.
[5] M. Guo, P. Ma, J. Wang, H. Xu, K. Zheng, D. Cheng, Y. Liu, G. Guo, H. Dai, E. Duan, J. Deng, Angew. Chem. Int. Ed. (2022), https://doi.org/10.1002/anie.202203827.
[6] E. Yu, J. Li, J. Chen, J. Chen, Z. Hong, H. Jia, J. Hazard. Mater. 388 (2020), 121800.
[7] J.C. Yu, L. Zhang, J. Yu, Chem. Mater. 14 (2002) 4647–4653.
[8] Y. Guo, M. Wen, G. Li, T. An, Appl. Catal. B: Environ. 281 (2021), 119447.
[9] Y. Feng, L. Dai, Z. Wang, Y. Peng, E. Duan, Y. Liu, L. Jing, X. Wang, A. Rastegarpanah, H. Dai, J. Deng, Environ. Sci. Technol. 56 (2022) 8722–8732.
[10] L. Kang, X.Y. Liu, A. Wang, L. Li, Y. Ren, X. Li, X. Pan, Y. Li, X. Zong, H. Liu, A. I. Frenkel, T. Zhang, Angew. Chem. Int. Ed. 132 (2020) 13009–13016.
[11] J. Kong, G. Li, M. Wen, J. Chen, H. Liu, T. An, J. Catal 370 (2019) 88–96.
[12] D. Wu, P.-F. Zhang, G.-P. Yang, L. Hou, W.-Y. Zhang, Y.-F. Han, P. Liu, Y.-Y. Wang, Coordin. Chem. Rev. 434 (2021), 213709.
[13] E.A. Dolgopolova, A.M. Rice, C.R. Martin, N.B. Shustova, Chem. Soc. Rev. 47 (2018) 4710–4728.
[14] X. Xu, Z. Zhang, X. Wang, Adv. Mater. 27 (2015) 5365–5371.

[15] Y. Guo, M. Wen, S. Song, Q. Liu, G. Li, T. An, Appl. Catal. B: Environ. 308 (2022), 121212.
[16] Y.-Z. Chen, R. Zhang, L. Jiao, H.-L. Jiang, Coordin, Chem. Rev. 362 (2018) 1–23.
[17] Y. Ma, L. Wang, J. Ma, H. Wang, C. Zhang, H. Deng, H. He, A.C.S. Catal 11 (2021) 6614–6625.
[18] Y. Jiang, J. Gao, Q. Zhang, Z. Liu, M. Fu, J. Wu, Y. Hu, D. Ye, Chem. Eng. J. 371 (2019) 78–87.
[19] M. Dan-Hardi, C. Serre, T. Frot, L. Rozes, G. Maurin, C. Sanchez, G. Férey, J. Am. Chem. Soc. 131 (2009) 10857–10859.
[20] J. Dou, Y. Li, F. Xie, X. Ding, M. Wei, Cryst. Growth Des. 16 (2016) 121–125.
[21] Z. Wang, X. Li, H. Xu, Y. Yang, Y. Cui, H. Pan, Z. Wang, B. Chen, G. Qian, J. Mater. Chem. A 2 (2014) 12571–12575.
[22] Z. Guo, J.K. Cheng, Z. Hu, M. Zhang, Q. Xu, Z. Kang, D. Zhao, R.S.C. Adv 4 (2014) 34221–34225.
[23] N.D. McNamara, J. Kim, J.C. Hicks, Energy Fuels 30 (2016) 594–602.
[24] Y. Gu, K. Cheng, Y. Y.-n. Wu, C. Wang, F.Li Morlay, ACS Sustain. Chem. Eng. 4 (2016) 6744–6753.
[25] J. Wang, L. Dai, J. Deng, Y. Liu, L. Jing, X. Hao, W. Pei, X. Yu, A. Rastegarpanah, H. Dai, Appl. Catal. B: Environ. 296 (2021), 120361.
[26] M. Faycal Atitar, A.A. Ismail, S.A. Al-Sayari, D. Bahnemann, D. Afanasev, A. V. Emeline, Chem. Eng. J. 264 (2015) 417–424.
[27] C. Zhao, Z. Wang, X. Chen, H. Chu, H. Fu, C.-C. Wang, Chin. J. Catal. 41 (2020) 1186–1197.
[28] X. Liu, Q. Han, W. Shi, C. Zhang, E. Li, T. Zhu, J. Catal 369 (2019) 482–492.
[29] N. Kamiuchi, T. Mitsui, H. Muroyama, T. Matsui, R. Kikuchi, K. Eguchi, Appl. Catal. B: Environ. 97 (2010) 120–126.
[30] K. Inoue, S. Somekawa, Chem. Eng. Technol. 42 (2019) 257–260.
[31] S.S.T. Bastos, S.A.C. Carabineiro, J.J.M. Órfão, M.F.R. Pereira, J.J. Delgado, J. L. Figueiredo, Catal. Today 180 (2012) 148–154.
[32] Y. Xia, L. Xia, Y. Liu, T. Yang, J. Deng, H. Dai, J. Environ. Sci. 64 (2018) 276–288.
[33] L.-Y. Jin, R.-H. Ma, J.-J. Lin, L. Meng, Y.-J. Wang, M.-F. Luo, Ind. Eng. Chem. Res. 50 (2011) 10878–10882.
[34] N. Perkas, H. Rotter, L. Vradman, M.V. Landau, A. Gedanken, Langmuir 22 (2006) 7072–7077.
[35] M. Ma, R. Yang, C. He, Z. Jiang, J.-W. Shi, R. Albilali, K. Fayaz, B. Liu, J. Hazard. Mater. 401 (2021), 123281.
[36] X. Wen, W. Li, J. Yan, X. Wang, E. Ren, Z. Shi, J. Li, X. Ding, S. Mo, D. Mo, J. Phys. Chem. C. 126 (2022) 1450–1461.
[37] Y. Qin, F. Shen, T. Zhu, W. Hong, X. Liu, R.S.C. Adv 8 (2018) 33425–33431.
[38] T. Mitsui, T. Matsui, R. Kikuchi, K. Eguchi, Top. Catal. 52 (2009) 464–469.
[39] C. He, P. Li, J. Cheng, Z.-P. Hao, Z.-P. Xu, Water Air Soil Pollut. 209 (2010) 365–376.
[40] Z. Hou, L. Dai, J. Deng, G. Zhao, L. Jing, Y. Wang, X. Yu, R. Gao, X. Tian, H. Dai, D. Wang, Y. Liu, Angew. Chem. Int. Ed. (2022), https://doi.org/10.1002/anie.202201655.
[41] X. Yu, L. Dai, J. Deng, Y. Liu, L. Jing, X. Zhang, R. Gao, Z. Hou, L. Wei, H. Dai, Appl. Catal. B: Environ. 305 (2022), 121037.
[42] Z. Wang, P. Ma, K. Zheng, C. Wang, Y. Liu, H. Dai, C. Wang, H.-C. Hsi, J. Deng, Appl. Catal. B: Environ. 274 (2020), 118963.
[43] Y. Song, N. Li, D. Chen, Q. Xu, H. Li, J. He, J. Lu, A.C.S. Sustainable, Chem. Eng. 6 (2018) 4000–4007.
[44] J.A. Rengifo-Herrera, E. Mielczarski, J. Mielczarski, N.C. Castillo, J. Kiwi, C. Pulgarin, Appl. Catal. B: Environ. 84 (2008) 448–456.
[45] O. Elbanna, P. Zhang, M. Fujitsuka, T. Majima, Appl. Catal. B: Environ. 192 (2016) 80–87.
[46] C. Zhang, Y. Zhou, J. Bao, X. Sheng, J. Fang, S. Zhao, Y. Zhang, W. Chen, ACS Appl. Mater. Interfaces 10 (2018) 18796–18804.
[47] Y. Feng, C. Wang, C. Wang, H. Huang, H.-C. Hsi, E. Duan, Y. Liu, G. Guo, H. Dai, J. Deng, J. Hazard. Mater. 424 (2022), 127337.
[48] X. Yu, L. Dai, J. Deng, Y. Liu, L. Jing, X. Zhang, X. Jiang, Z. Hou, J. Wang, H. Dai, J. Catal 400 (2021) 310–324.
[49] Z. Hou, L. Dai, Y. Liu, J. Deng, L. Jing, W. Pei, R. Gao, Y. Feng, H. Dai, Appl. Catal. B: Environ. 285 (2021), 119844.
[50] C. Rettenmaier, R.M. Arán-Ais, J. Timoshenko, R. Rizo, H.S. Jeon, S. Kühl, S. W. Chee, A. Bergmann, B. Roldan Cuenya, A.C.S. Catal 10 (2020) 14540–14551.
[51] W. Pei, L. Dai, Y. Liu, J. Deng, L. Jing, K. Zhang, Z. Hou, Z. Han, A. Rastegarpanah, H. Dai, J. Catal 385 (2020) 274–288.
[52] Y. Huang, M. Tian, Z. Jiang, M. Ma, C. Chen, H. Xu, J. Zhang, R. Albilali, C. He, Appl. Catal. B: Environ. 304 (2022), 121002.
[53] S. Song, S. Zhang, X. Zhang, P. Verma, M. Wen, Front, Mater 7 (2020), 595667.
[54] L. Wu, J. Deng, Y. Liu, L. Jing, X. Yu, X. Zhang, R. Gao, W. Pei, X. Hao, A. Rastegarpanah, D. Hongxing, J. Environ. Sci. 116 (2022) 209–219.
[55] Y. Huo, Y. Jin, J. Zhu, H. Li, Appl. Catal. B: Environ. 89 (2009) 543–550.
[56] S. Li, Y.H. Ng, R. Zhu, S. Lv, C. Wu, Y. Liu, L. Jing, J. Deng, H. Dai, Appl. Catal. B: Environ. 297 (2021), 120412.
[57] S. Lv, Y.H. Ng, R. Zhu, S. Li, C. Wu, Y. Liu, Y. Zhang, L. Jing, J. Deng, H. Dai, Appl. Catal. B: Environ. 297 (2021), 120438.
[58] K. Wang, T. Peng, Z. Wang, H. Wang, X. Chen, W. Dai, X. Fu, Appl. Catal. B: Environ. 250 (2019) 89–98.
[59] H. Wang, S. Chen, Z. Wang, Y. Zhou, Z. Wu, Appl. Catal. B: Environ. 254 (2019) 339–350.
[60] T.K. Phung, A.A. Casazza, B. Aliakbarian, E. Finocchio, P. Perego, G. Busca, Chem. Eng. J. 215–216 (2013) 838–848.
[61] T. Pan, H. Deng, S. Kang, Y. Zhang, W. Lian, C. Zhang, H. He, Chem. Eng. J. 417 (2021), 129246.
[62] L. Wang, Y. Yi, C. Wu, H. Guo, X. Tu, Angew. Chem. Int. Ed. 129 (2017) 13867–13871.
[63] M.R. Nimlos, E.J. Wolfrum, M.L. Brewer, J.A. Fennell, G. Bintner, Environ. Sci. Technol. 30 (1996) 3102–3110.
[64] Y. Zeng, X. Luo, F. Li, A. Huang, H. Wu, G.Q. Xu, S.L. Wang, Environ. Sci. Technol. 55 (2021) 7711–7720.
[65] Y. Shen, J. Deng, S. Impeng, S. Li, T. Yan, J. Zhang, L. Shi, D. Zhang, Environ. Sci. Technol. 54 (2020) 10342–10350.
[66] X.-H. Yi, S.-Q. Ma, X.-D. Du, C. Zhao, H. Fu, P. Wang, C.-C. Wang, Chem. Eng. J. 375 (2019) 121944.
[67] X. Zhang, Y. Liu, J. Deng, L. Jing, X. Yu, Z. Han, H. Dai, Catal. Today 375 (2021) 623–634.